Journal of
Synchrotron Radiation
ISSN 0909-0495

Received 23 February 2006
Accepted 1 June 2006

Combustion front dynamics in the combustion synthesis of refractory metal carbides and di-borides using time-resolved X-ray diffraction

Joe Wong,[a]* E. M. Larson,[b] P. A. Waide[a] and R. Frahm[c]

[a]Lawrence Livermore National Laboratory, University of California, PO Box 808, Livermore, CA 94551, USA, [b]College of Science and Allied Health, Grand Canyon University, 3300 West Camelback Road, Phoenix, AZ 85017, USA, and [c]Department of Physics, Bergische Universität Wuppertal, Gaußstr. 20, D-42097 Wuppertal, Germany. E-mail: exafs_materials@sbcglobal.net

A compact diffraction-reaction chamber, using a 2-inch photodiode array detector, has been employed to investigate the chemical dynamics at the combustion front of a selected series of refractory metal carbides and di-borides from their constituent element reactants as well as binary products from B_4C as a reactant. These systems are denoted as (i) $M + C \rightarrow MC$; (ii) $M + 2B \rightarrow MB_2$; and (iii) $3M + B_4C \rightarrow 2MB_2 + MC$, where M = Ti, Zr, Nb, Hf or Ta. Time-resolved X-ray diffraction using intense synchrotron radiation at frame rates up to 10 frames s^{-1} (or 100 ms frame^{-1}) was employed. The combustion reactions were found to complete within 200–400 ms. In contrast to the Ta + C $\rightarrow$ TaC combustion system studied earlier, in which a discernible intermediate sub-carbide phase was first formed, reacted further and disappeared to yield the final TaC product, no intermediate sub-carbide or sub-boride was detected in the current systems. Combustion for the Ti, Zr and Hf systems involved a liquid phase, in which the adiabatic temperatures T_{ad} are well above the melting points of the respective reactant metals and have a typical combustion front velocity of 5–6 mm s^{-1}. The Nb and Ta systems have lower T_{ad}, involving no liquid phase. These are truly solid combustion systems and have a lower combustion front velocity of 1–2 mm s^{-1}. The current study opens up a new avenue to chemical dynamics and macrokinetic investigations of high-temperature solid-state reactions.

Keywords: time-resolved X-ray diffraction; combustion synthesis; metal carbides; metal di-borides.

1. Introduction

Combustion synthesis is a relatively novel crucible-less process for preparing high-temperature materials *via* solid-state reactions. Once ignited with an external source such as a laser or an electrically heated tungsten coil, these combustion reactions are universally accompanied by the release of a large amount of heat, become self-sustaining, and propagate to completion within seconds. This field of study was pioneered by Russian workers and in the former Soviet Union about three decades ago (Merzhanov & Borovinskaya, 1972; Merzhanov, 1974) and has been coined self-propagating high-temperature synthesis by the Russian school (Naiborodenko & Itin, 1975; Aleksandrov & Korchagin, 1987) or simply called solid combustion syntheses (SCS) reactions (Munir & Holt, 1990). These reactions are characterized by a fast-moving combustion front (1–100 mm s^{-1}) and a self-generated high temperature (1000–4000 K) under adiabatic conditions (Merzhanov, 1990*a*,*b*). A number of ceramic, intermetallic and composite materials have been synthesized by this method (Hirao *et al.*, 1987; Yamada *et al.*, 1987; Munir, 1988; Munir & Anselmi-Tamburini, 1989), including high-temperature superconducting oxides (Merzhanov, 1990*a*,*b*; Lebrat & Varma, 1991; Rupp *et al.*, 1994). More recently, the influence of an electric field on the combustion synthesis of metal silicides has been investigated by Munir and co-workers (Feng & Munir, 1995; Gedevanishvili & Munir, 1995; Xue & Munir, 1996; Shon *et al.*, 1996).

In combustion synthesis, high-intensity heat sources are used to initiate an exothermic reaction within a small region of material creating a combustion front. The high-temperature combustion front induces solid-state reactions and/or phase transformations along its path of propagation and may also cause melting and solidification in regions of the material where the liquidus temperature has been exceeded. This is depicted in Fig. 1, which shows schematically the various heat-

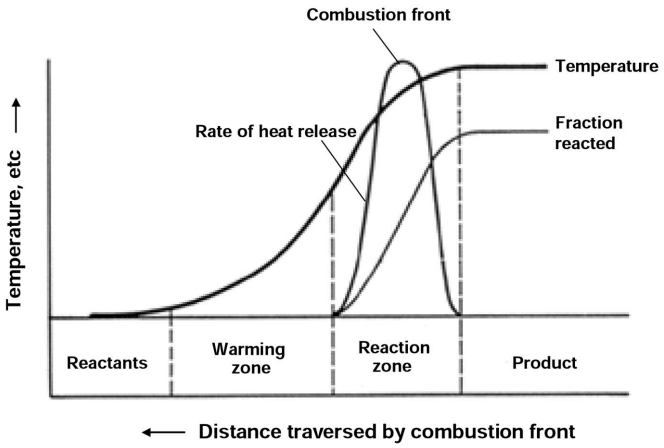

Figure 1
Schematic diagram showing a linear combustion front and various heat-affected regions of a solid undergoing combustion synthesis. The distance and direction traversed by the combustion front (right to left) which creates the various zones along the sample at a given time is depicted along the x axis. The temperature, rate of heat release and fraction of reactant converted are plotted vertically in arbitrary scales (adapted from Merzhanov, 1990*a*).

affected and reaction regions of the material during the passage of the combustion front.

Although the basic concepts of this method of materials synthesis are relatively easy to apply in principle, there remain a number of fundamental questions concerning the physical and chemical nature as well as the dynamics of reaction and phase transformation within the moving combustion front. Real-time studies of dynamical processes *in situ* under severe temperature or pressure conditions often pose a challenge for experimentalists. The situation is true even with the most simple $A + B \rightarrow AB$ combustion reactions. Until recently, it has been difficult to investigate these reactions because of the speed and extreme thermal conditions (Boldyrev & Aleksandrov, 1981; Wong *et al.*, 1990; Frahm *et al.*, 1992; Larson *et al.*, 1993; Rupp *et al.*, 1994). Conventionally, examinations of reactant and product phases and their microstructures are possible with X-ray diffraction and a variety of optical and electron microscopies in a *post mortem* fashion. However, the high temperature, confined reaction region (sub-mm) and fast rates of combustion preclude any *in situ* investigation of structural changes and chemical dynamics in the combustion zone in real time and real space (sample position) with most conventional techniques.

In this paper we employ our time-resolved diffraction technique developed earlier to study the combustion syntheses of NiAl (Wong *et al.*, 1990) and TaC (Larson *et al.*, 1993), and apply a refined compact diffraction-reaction chamber to study the combustion synthesis of some selective refractory metal carbides and di-borides both as a single product as well as binary composite products. These reactions are typified by (i) $M + C \rightarrow MC$; (ii) $M + 2B \rightarrow MB_2$; and (iii) $3M + B_4C \rightarrow 2MB_2 + MC$, where M = Ti, Zr, Nb, Hf or Ta. The choice of these refractory carbide and di-boride combustion reactions is twofold. First, their reaction products are fairly simple from the X-ray diffraction point of view. The metal carbides all have a NaCl cubic structure and the metal di-borides have an AlB_2 hexagonal structure (Wyckoff, 1964) with known X-ray diffraction patterns (Villars & Calvert, 1985). Secondly, with increasing atomic number from 3*d* to 4*d* and to 5*d* metals, the X-ray scattering power, and hence the diffracted intensity, increases to enable good time resolution down to 100 ms or even better.

2. Experimental

2.1. Time-resolved X-ray diffraction (TRXRD) measurements

The apparatus consists of a compact controlled-atmosphere diffraction chamber, a two-inch X-ray photodiode array detector system (Princeton Instruments) and a scanning infrared pyrometer (Inframetrics). These components are shown schematically in Fig. 2. The X-ray detector is mounted on the chamber so as to cover a 30° span of 2θ space centered at 40° 2θ. The detector doubles the 2θ range of the 1-inch detector array used previously (Wong *et al.*, 1990; Larson *et al.*, 1991). With this design the detector can record most of the high-intensity diffraction lines of a large variety of crystalline substances to facilitate phase identification in the course of reactions. A KBr infrared viewport is incorporated in the chamber for real-time temperature profile measurement synchronously with the diffraction scans. A dedicated PC computer is used to run the experiment, trigger the detector, and collect diffraction data as a function of time as short as 10 ms.

The chamber can operate under vacuum, or can be back-filled with various gases, either inert or reactive, at partial pressures up to 1 atm. A small stationary area of the sample is illuminated with X-rays. The sample holder was made of stainless steel and lined with a grafoil sheet to protect it from corrosion by the hot specimen during combustion. The sample was supported by four carbide cutter bits as shown in Fig. 3.

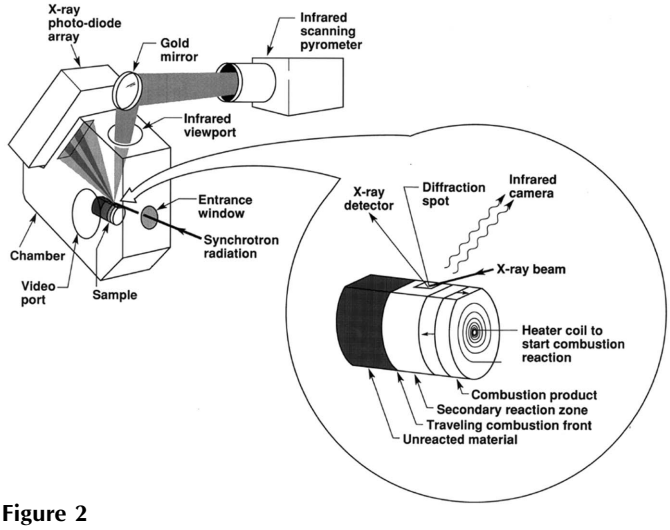

Figure 2
Schematic diagram for the TRXRD diffraction-chamber and IR pyrometer used in this study. The inset is an enlargement detailing the various regions of the sample during combustion synthesis shown photographically in Fig. 3.

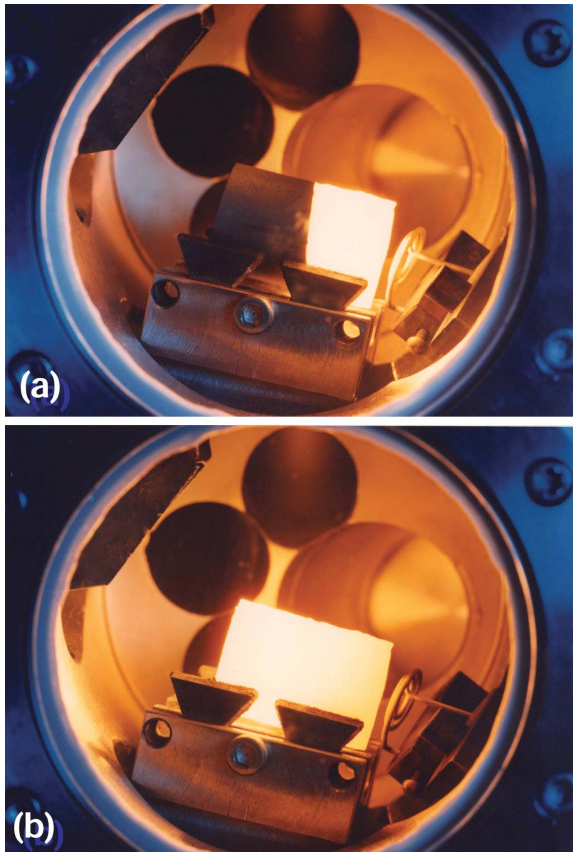

Figure 3
Time-lapsed photographs for the combustion synthesis of Zr + C → ZrC in the diffraction–reaction chamber: (*a*) half-way through the combustion after ignition with the tungsten coil powered off, and (*b*) at completion of combustion. The combustion front was moving from right to left at a velocity of 5.8 mm s^{-1} as recorded with a video camera.

The sample support along lines using materials of low thermal conductivity and minimal thermal contact area ensured adiabatic conditions in the sample. The sample scatters (diffracts) the X-rays in a pattern characteristic of its crystal structure under the reaction conditions of temperature and pressure at a given time interval of the combustion. The diffracted X-rays pass out of the chamber through a thin Mylar exit window and are collected by the position-sensitive photodiode array detector. The detector is capable of recording a full scan of 2048 pixels in as little as 8 ms or 125 scans s^{-1}. The solid combustion reactions are initiated by passing current through a tungsten coil adjacent to the pressed sample block. This is shown in a laboratory run of the ZrC synthesis given in Fig. 3. Fig. 3(*a*) shows the propagation of the combustion front about half way along the cylindrical specimen of equimolar powder mixture of Zr and C. The tungsten coil to the right was turned off right after the reaction (combustion) became self-sustaining. Fig. 3(*b*) is a photograph taken just after the combustion front reached the end of the specimen. The length of the reactant specimen was ∼20 mm and the reaction was completed within 3.5 s with a combustion front velocity of 5.8 mm s^{-1}. The photographs in Fig. 3 were frames extracted from a video recording (SONY Video-8). Data collection is triggered by the computer prior to the arrival of the combustion front at the sample area illuminated by the X-ray beam (see Fig. 2 inset). The diffraction peaks within the 30° 2θ window space were recorded at a pre-selected rate of 100 ms $scan^{-1}$ and total scan time of 50 s.

TRXRD experiments were performed at Brookhaven National Synchrotron Light Source (NSLS) on beamline X-11A (Heald *et al.*, 1986). The storage ring was operated at an electron energy of 2.528 GeV and an injection current of ∼180 mA. The synchrotron beam, 2 mrad, was passed through a 1 mm entrance slit and was monochromated with a double Si(111) crystal at 8 keV (1.5497 Å) and then focused. The vertical hutch slit was adjusted to a height of 0.25 mm. This produced an X-ray beam of width 0.6 mm, perpendicular to the length of the sample at an angle $\theta \simeq 25°$ and at a right-angle to the combustion front. Diffraction patterns were collected and stored at constant time intervals from the initiation of the reaction through completion with a total collection time ranging from 15 to 100 s. A typical TRXRD experiment might consist of 600 scans each collected at 100 ms. Scan times of 50, 100 and 200 ms per frame were also used. Data sets were collected during the burns of several samples of each mixture. Some expansion of the material was expected and took place during the reaction causing slight shifts in the peak positions in 2θ value, which could be tracked in the scans. Prior to ignition, the room-temperature diffraction pattern of each specimen was routinely recorded to optimize sample position, choice of 2θ window and signal-to-noise ratios with scan time. Diffraction scans were also taken of the cooled product 5–10 min after completion of the reaction. Conventional powder diffraction patterns from the surface as well as the interior of each of the reacted samples were later collected in the laboratory to verify the product phase using a conventional X-ray tube.

2.2. Inframetric pyrometry

The temperature of the specimen was recorded concurrently with the TRXRD measurements using an infrared camera (Inframetrics, Model 600) through a KBr window. The specimen temperature at a pixel location up-burn from the X-ray target area was compared with a preset trigger temperature (say, 373 K). As soon as the measured value reached or exceeded the trigger temperature, a signal was sent to the detector controller and the diffraction data collection was activated. This trigger set the time at zero for each series of TRXRD patterns. The placement and orientation of the infrared optics path allowed the pyrometer to record the surface temperature at the diffraction region of the sample (see Fig. 2) in a conventional video imaging mode at 30 frames s^{-1}, or as an infrared streak camera at 8000 lines s^{-1}. In the imaging mode the pyrometer produced a two-dimensional image of the diffraction region in which the image intensity values could be converted digitally to temperature values. This mode gives temperature values for the entire sample with fairly good time resolution. For particularly fast reactions or phase transformation, the fast line-scan (streak camera) mode was used. Instead of a two-

dimensional image, it records intensities as a function of x and time, where the x axis is aligned with the direction of burn front motion. Only a single video line across the sample is measured, but the measurements are performed at a much higher rate. As with the imaging mode, the line-scan intensity values can be converted digitally to yield temperature values as a function of position and time. The temperature values obtained in either mode can be correlated to the corresponding X-ray diffraction scans to give the local temperature, physical state and chemical composition of a sample at very high time resolution. To obtain adequate spatial resolution, a 3× Ge telephoto lens together with a 12-inch focal-length Ge close-up lens (both by Inframetrics) were used. Each image pixel corresponds to a 133 μm × 133 μm region on the sample. He, a monatomic gas, was used to fill the chamber to minimize heat transfer to the chamber *via* convective loss in order to preserve adiabatic conditions.

Table 1
Summary of combustion reactions and their characteristics investigated in this work.

Reaction	Velocity (mm s^{-1})	Adiabatic temperature (K)	Integration time/frame (ms)	Reaction time (s)	Liquid phase
Ti + C → TiC	5.0	3200	200	0.4	Yes (Ti)
Zr + C → ZrC	5.8	3758	100	0.3	Yes (Zr)
Hf + C → HfC	6.0	3900	100	0.2	Yes (Hf)
Zr + 2B → ZrB_2	5.0	3223	200	0.4	Yes (Zr)
Nb + 2B → NbB_2	1.0	2251	100	0.3	No
Hf + 2B → HfB_2	5.0	3083	100	0.2	Yes (Hf)
3Zr + B_4C → 2ZrB_2 + ZrC	6.4	3156	200	0.6	Yes (Zr)
3Hf + B_4C → 2HfB_2 + HfC	5.0	3103	100	0.2	Yes (Hf)
3Ta + B_4C → 2TaB_2 + TaC	2.0	2476.	100	0.6	No

2.3. Preparation of combustion synthesis specimens

Stoichiometric mixtures of metal and carbon, metal and boron and metal and B_4C powders (1:1, 1:2 and 3:1) for reactions M + C, M + 2B and 3M + B_4C, respectively, were weighed, mechanically mixed and homogenized in a SPEX mixer for 10–30 min. The combustion specimens were pressed cylindrical pellets, 20 mm in diameter and about 25 mm long with a green density of ∼55%. All powders were supplied commercially by Cerac and were −325 mesh or finer in particle size with a purity of 99.95%. The pressed samples were ignited at one end with a resistively heated tungsten coil (Fig. 3*a*). Current to the tungsten coil was turned off when the combustion reaction became self-sustaining due to the highly exothermic nature of the reaction (see Table 1). All combustion reactions reported here were performed in helium at a pressure of 1 atm or slightly less to obviate oxidation and to minimize air attenuation of the X-ray beam and, hence diffraction signals.

3. Results and discussion

3.1. Combustion front velocity

The velocity of the combustion front is a characteristic feature of an SCS reaction system. It is a function of the reaction type, powder particle size, green density, overall dimensions, ambient atmosphere, initial temperature, presence of liquid phase *etc.* The combustion front velocities of the various refractory metal carbides and di-borides syntheses used in the present TRXRD study are given in Table 1. A SONY Video-8 camera was used to record the velocity. An arc welder glass was used to filter the glare from the white glowing combusting specimen at high temperature during passage of the combustion front. All combustion fronts studied here were linear. The adiabatic temperatures T_{ad} (assuming no heat loss) for each of the reactions were also calculated using known thermodynamic values for heat capacities, heats of formation, fusion *etc.* (Barin & Knacke, 1973; Barin *et al.*, 1977), according to a procedure prescribed by the program *ADIBAT* (Rupp *et al.*, 1992).

These calculated adiabatic temperatures for the single carbide and di-boride combustions are within ±200 K of those given in the literature (Novikov *et al.*, 1975). The discrepancy might be due to sources of the thermodynamic data used. Except for the NbB_2 and Ta systems, the combustion fronts of these refractory metal carbides and di-borides fall in the range 5–6 mm s^{-1} and with high corresponding T_{ad} values above 3000 K. The lower combustion fronts for the Nb and Ta systems show also lower T_{ad} values, reflective of the higher activation energies associated with these combustion reactions.

3.2. Combustion synthesis of metal carbides

3.2.1. Ti + C → TiC combustion. Fig. 4 shows a series of selected time-resolved diffraction patterns for the synthesis of TiC from a stoichiometric mixture of its constituent elements. In this TRXRD experiment, two 1-inch detectors, similar to the set-up used for the Ta + C combustion reported earlier (Larson *et al.*, 1993), were used. The detector integration time per diffraction pattern (scan) was 200 ms, and 500 such scans were recorded yielding a total measurement time of 100 s. From these 500 scans, seven representative individual scans were plotted in Fig. 4 to demonstrate the sequence of critical events during the Ti + C combustion. At t = 0.0 s, the detectors were triggered and recorded the reactant Ti(002) and Ti(101) peaks at ∼373 K (triggering temperature). The intensities of these diffractions persisted over the next second interval, and decreased abruptly at t = 1.2 s, indicative of the arrival of the combustion front and reaction at the X-ray irradiated region. The next frame, at t = 1.4 s, showed the emergence of the cubic product TiC(200) and (220) peaks, which grew at t = 1.6 s and moved to high 2θ values due to lattice contraction of the TiC product as the specimen cooled. Thus the Ti + C → TiC combustion took place and completed within 0.4 s with no discernible intermediates. This is further exemplified by a concentration profile plot of Ti and TiC, shown in Fig. 5, using the normalized intensities of the measured Ti and TiC Bragg peaks as a function of reaction time. The lower-than-expected 0.5 crossover point between the Ti reactant and TiC product

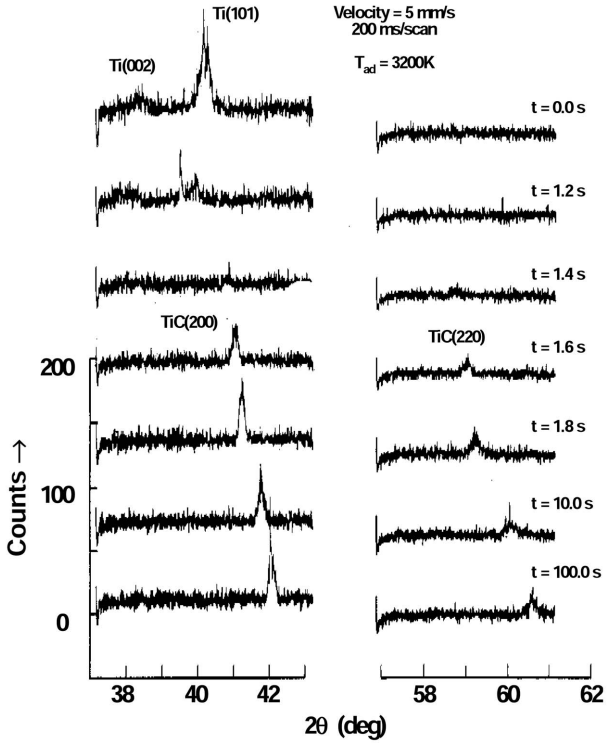

Figure 4
TRXRD patterns for the Ti + C → TiC reaction, showing the sequence of critical events during the combustion. Two 1-inch detectors (Larson *et al.*, 1991) similar to those used in the Ta + C system were used.

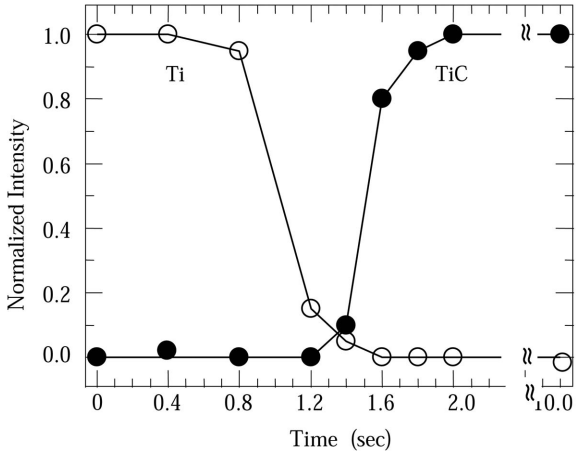

Figure 5
Normalized integrated intensities plotted as a function of time for Ti(101) and TiC(200) Bragg peaks, showing the chemical changes as a function of time during the Ti + C → TiC combustion.

strongly suggests that the combustion involves a liquid Ti phase (m.p. = 1933 ± 10 K). The melting point of TiC is 3410 ± 90 K (Weast & Astle, 1982), which is higher than T_{ad} = 3200 K for the Ti + C combustion (Table 1).

3.2.2. Zr + C → ZrC combustion. Fig. 6 shows a series of selected TRXRD patterns for the Zr + C → ZrC combustion. Each scan was recorded in 100 ms using the 2-inch photodiode array detector. At t = 0.0 s, the pressed powder sample of Zr and graphite was ignited by the tungsten coil, and the detector was triggered to record the reactant Zr(100), Zr(002), Zr(101),

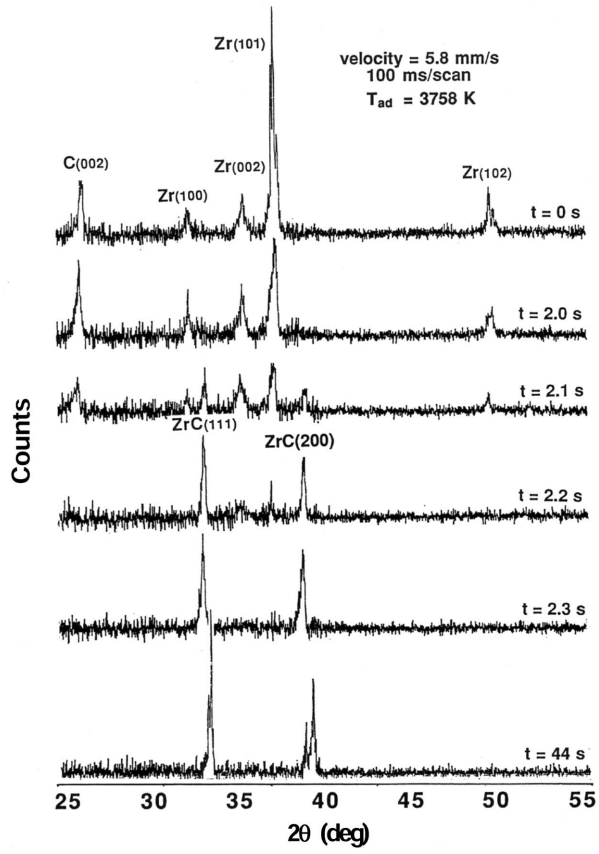

Figure 6
TRXRD patterns for the Zr + C → ZrC reaction, showing the sequence of critical events during the combustion. The new 2-inch photodiode array detector was used. The combustion was completed in 0.3 s.

Zr(102) and $C_{graphite}$(002) Bragg peaks at just above the room temperature. At t = 2.0 s, the combustion front traveled to the sample area illuminated by the synchrotron beam. Heating of the Zr + C mixed powder was detected by a drop in intensity of the major Zr(101) line due to thermal broadening (Debye–Waller effect). In the next frame, at t = 2.1 s, all Zr and C reactant peaks showed a decrease in intensity, and cubic ZrC product peaks began to emerge. At t = 2.2 s, the ZrC peaks became dominant with discernible Zr reactant peaks. At t = 2.3 s and onwards, the reactant peaks had all disappeared and both ZrC(111) and ZrC(200) peaks shifted to higher 2θ values, denoting lower interatomic spacings, and hence lattice contraction due to sample cooling all the way to t = 44.0 s. The total reaction time for this system was 0.3 s. No intermediate phases appeared in the diffraction data.

For each frame of TRXRD data, a corresponding thermal profile can be extracted from the infrared imaging or streak data. Owing to the lack of emissivity data at high temperature, we derived the temperature using an emissivity value of 1. Fig. 7 shows a series of temperature profiles of the Zr + C combustion front as it traversed to the X-ray illuminated region of the sample. The scans are plotted at 100 ms intervals. The profiles were recorded in the streak camera mode at 8000 sweeps per second (8 kHz). It is seen that the overall profiles were quite uniform with time, peaking at ∼2873 K, which is

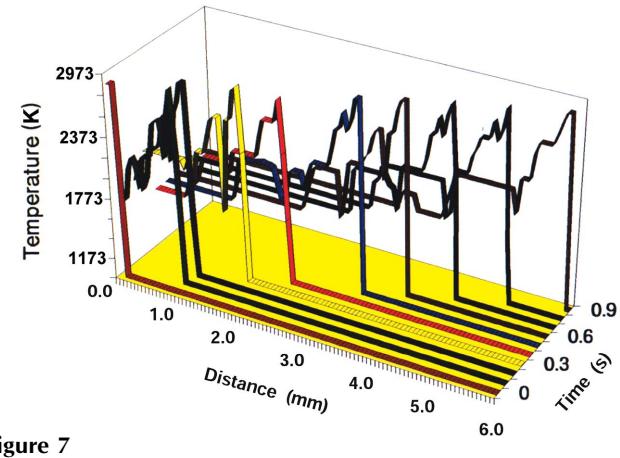

Figure 7
Time-resolved thermal profiles for the Zr + C → ZrC combustion, measured using the Inframetric camera in a streak mode at 8 kHz. The recorded peak temperature of ∼2873 K indicates that the Zr metal reactant (m.p. = 2128 K) was likely molten during passage of the combustion front.

almost 900 K below a calculated adiabatic temperature of 3758 K for this reaction. This is, no doubt, due to heat loss arising from radiation, convection and conduction in the reaction chamber. From these profiles it is evident that the Zr powder (m.p. = 2128 K) melted at the combustion front (reaction zone), but not graphite, which has a sublimation point at ∼3925 K (Weast & Astle, 1982).

3.2.3. Hf + C → HfC combustion. Fig. 8 shows a series of selected TRXRD patterns for the Hf + C → HfC combustion. Each scan was recorded in 100 ms with the 2-inch photodiode array detector. At t = 0.0 s, the pressed powder sample of Hf and graphite was ignited by the tungsten coil, and the detector was triggered to record the reactant $C_{graphite}(002)$, Hf(100), Hf(002), Hf(101) and Hf(102) Bragg peaks at just above room temperature. At t = 1.40 s, the combustion front traveled to the sample area illuminated by the synchrotron beam and caused a change in the diffraction geometry (sample movement) as well as intrinsic lattice expansion to yield an overall peaks shifts to high 2θ. In the next frame at t = 1.5 s, all Hf and C reactant peaks showed a decrease in intensity accompanied by the appearance of the cubic HfC(111) and HfC(200) peaks. At t = 1.6 s and onwards, the reactant peaks had all disappeared and both of the HfC product peaks shifted to higher 2θ values, due to lattice contraction as the sample cooled all the way to t = 40.0 s. This reaction occurred and completed within 0.2 s, also with no detectable intermediates. Melting of the Hf metal is expected since its melting point (2500 K) is well below the 3900 K adiabatic temperature for the Hf + C combustion (Table 1). The HfC formed as a solid since its melting point (at ∼4163 K; Weast & Astle, 1982) was above T_{ad}.

3.3. Combustion synthesis of metal di-borides

3.3.1. Zr + 2B → ZrB_2 combustion. Preliminary diffraction scans of the Zr + B (amorphous) powder mixture at room temperature yielded low-intensity patterns. Hence, an integration time of 200 ms was used for each frame of a TRXRD scan. Fig. 9 shows a series of selected TRXRD patterns for this

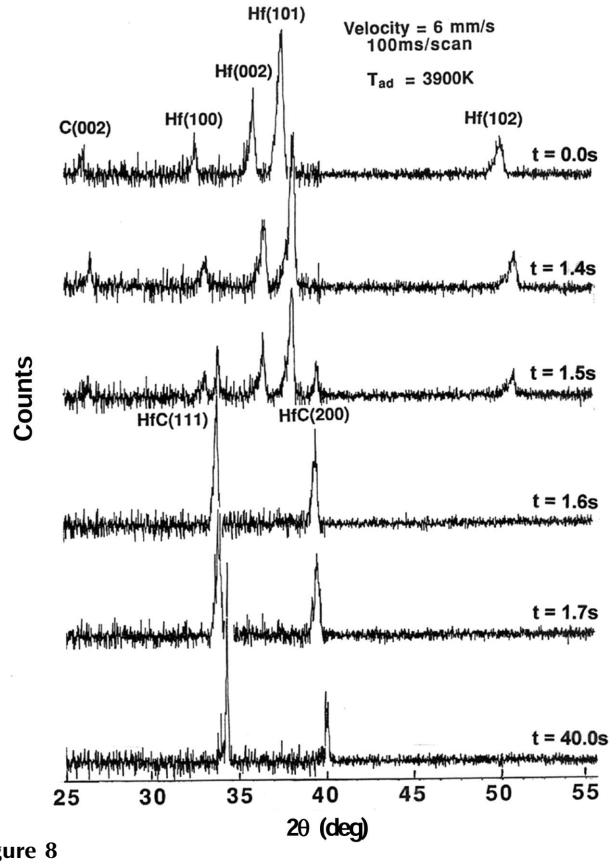

Figure 8
TRXRD patterns for the Hf + C → HfC reaction, showing the sequence of critical events during the combustion. The combustion was completed in 0.2 s with no detectable intermediates.

combustion. The combustion front has a velocity of 6 mm s^{-1}. At t = 0.0 s, the pressed powder sample of Zr and graphite was ignited by the tungsten coil, and the detector was triggered to record the reactant Zr(100), Zr(002), Zr(101) and Zr(102) Bragg peaks at just above room temperature. At t = 2.6 s, the major Zr(101) peak broadened, indicative of heating due to the arrival of the combustion front in the sample area illuminated by the synchrotron beam. At t = 3.0 s, heating of the Zr + B mixed powder continued and Zr melted at t = 3.2 s. In the next frame, at t = 3.4 s, the $ZrB_2(100)$ and $ZrB_2(101)$ peaks appeared and persisted to the end of the combustion. T_{ad} of this combustion is 3323 K, which is well above the melting point (2128 K) of Zr metal. The combustion completed within 0.4 s.

3.3.2. Nb + 2B → NbB_2 combustion. The combustion front of this reaction has a relatively low velocity of 1 mm s^{-1}. Each frame of the TRXRD scan was recorded using a 100 ms integration time. Fig. 10 shows a series of selected TRXRD patterns for this combustion. At t = 0.0 s, the pressed powder sample of Zr and graphite was ignited by the tungsten coil, and the detector was triggered to record the body-centered cubic Nb(110) Bragg peak at just above room temperature. At t = 9.3 s, this metal peak decreased in intensity marking the arrival of the combustion front at the sample area illuminated by the synchrotron beam. At t = 9.4 s, the product $NbB_2(100)$ and $NbB_2(101)$ peaks emerged. The reactant and product co-

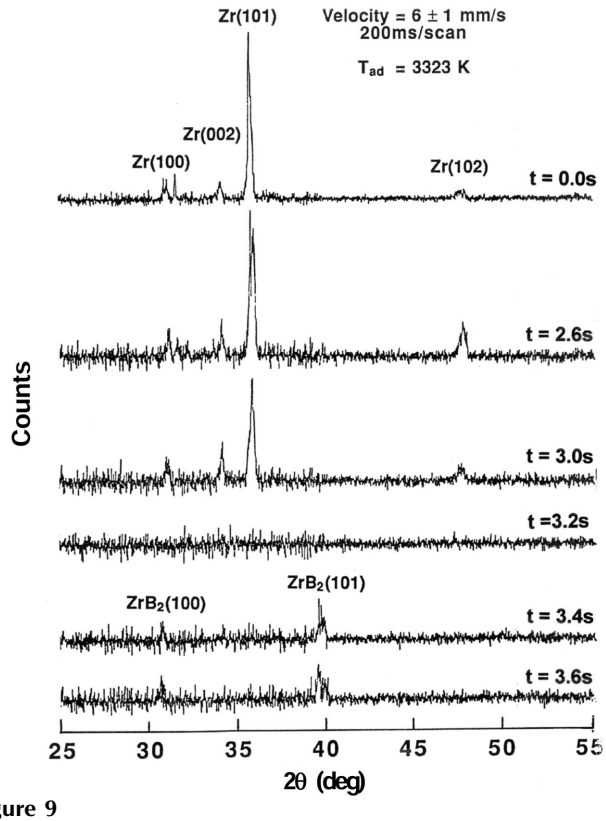

Figure 9
TRXRD patterns for the Zr + 2B → ZrB_2 reaction, showing the sequence of critical events during the combustion. The combustion was completed in 0.4 s. The frame at t = 3.2 s clearly indicates that the Zr metal was molten at the combustion (reaction) front.

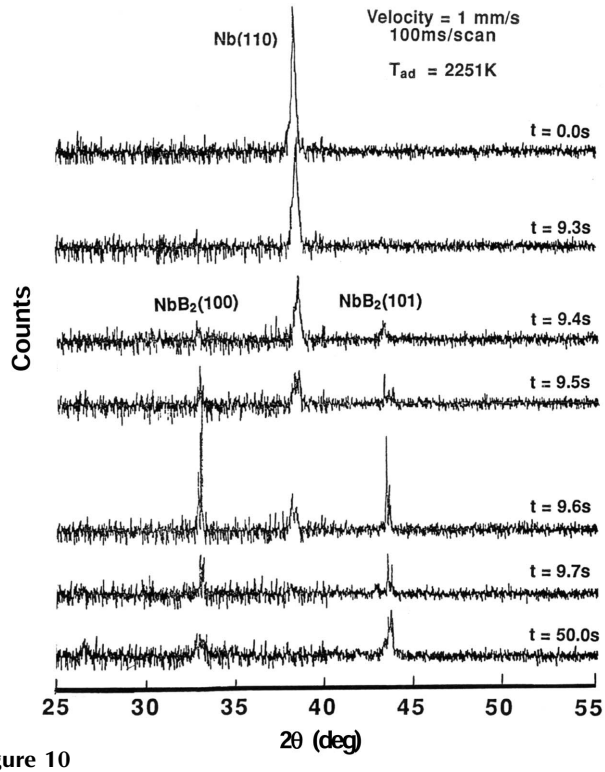

Figure 10
TRXRD patterns for the Nb + 2B → NbB_2 reaction, showing the sequence of critical events during the combustion. This reaction has a low combustion front of 1 mm s^{-1} and the combustion was completed in 0.3 s.

existed in the next 0.2 s. At t = 9.7 s and beyond, only the final product persisted. The reaction completed in 0.3 s. T_{ad} of this combustion is calculated to be 2251 K, which is well below the melting points of both Nb and B, at 2750 K and 2573 K (Weast & Astle, 1982), respectively. This is a case of true solid-state combustion, in which all reactants and combustion products are in the solid state. A similar solid-state combustion has been reported earlier for the case of Ta + C → TaC combustion (Larson *et al.*, 1993), which has a similarly low combustion front of ∼2 mm s^{-1}.

3.3.3. Hf + 2B → HfB_2 combustion. Because Hf is a 5*d* metal, an integration time of 100 ms was found adequate for the TRXRD scans for the Hf system. Fig. 11 shows a series of selected TRXRD patterns for this reaction. The combustion front has a velocity of 5 mm s^{-1}. At t = 0.0 s, the pressed powder sample of Hf + boron was ignited by the tungsten coil, and the detector was triggered to record the reactant Hf(100), Hf(002), Hf(101) and Hf(102) Bragg peaks at just above the room temperature. At t = 1.5 s, the major Hf(101) peak sharpened somewhat (anneal), marking the arrival of the combustion front at the sample area illuminated by the synchrotron beam. At t = 1.6 s, the Hf concentration decreased with the emergence of the product HfB_2(100) and HfB_2(101) peaks, which persisted solely at t = 1.8 s and beyond. The combustion completed in 0.2 s. T_{ad} of this combustion is 3083 K which is above the melting point of 2500 K for the Hf metal (Weast & Astle, 1982).

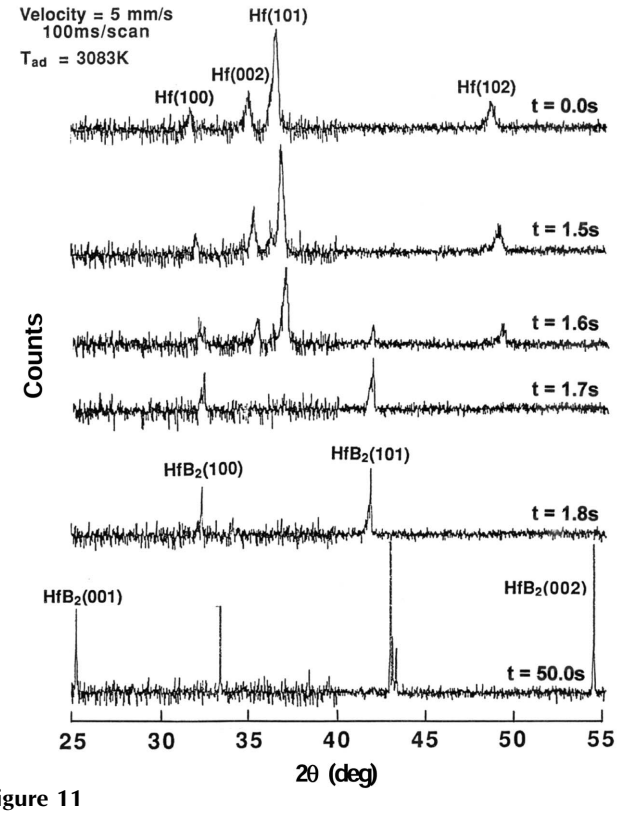

Figure 11
TRXRD patterns for the Hf + 2B → HfB_2 reaction, showing the sequence of critical events during the combustion. Hf metal melted and the combustion was completed in 0.2 s.

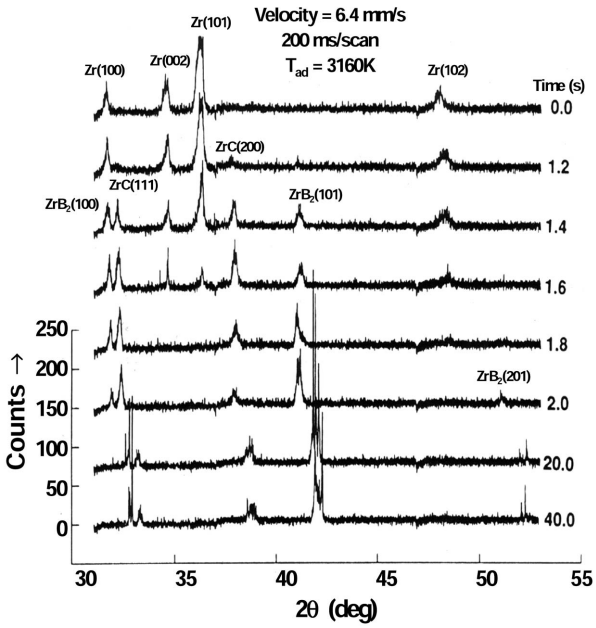

Figure 12
TRXRD patterns for the $3Zr + B_4C \rightarrow 2ZrB_2 + ZrC$ reaction, showing the sequence of critical events during the combustion. The combustion was completed within 0.6 s.

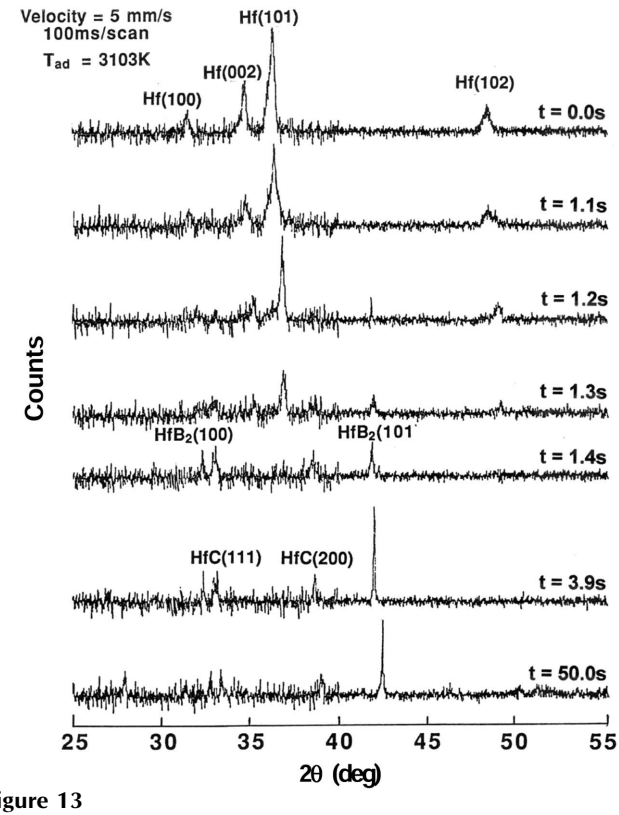

Figure 13
TRXRD patterns for the $3Hf + B_4C \rightarrow 2HfB_2 + HfC$ reaction, showing the sequence of critical events during the combustion. The combustion was completed within 0.2 s.

3.4. Combustion synthesis of metal di-boride–carbide composite

We have also studied the reaction dynamics for the binary synthesis of metal di-boride and carbide: $3M + B_4C \rightarrow 2MB_2 + MC$, where M = Zr, Hf and Ta. The results are described in the following.

3.4.1. $3Zr + B_4C \rightarrow 2ZrB_2 + ZrC$ combustion. From Table 1, the adiabatic temperature of this reaction is somewhat between those of the individual ZrC and ZrB_2 from the respective elements shown in §3.2.2 and §3.3.1. This reaction has a combustion front velocity of 6.4 mm s^{-1}. The TRXRD patterns are shown in Fig. 12. Each frame was recorded with an integration time of 200 ms. At t = 0.0 s, the reaction was triggered and the reactant Zr(100), Zr(002), Zr(101) and Zr(102) peaks were recorded at ∼373 K, the triggering temperature. The ZrC product first appeared at t = 1.2 s, co-existent with the Zr metal. Appearance of the ZrB_2 product is seen in the next frame, at t = 1.4 s, co-existent with both Zr and ZrC, which also persisted in the next frame at t = 1.6 s. From t = 1.8 s onwards, only the product peaks persisted, shifting to high 2θ values due to lattice contraction as the reacted sample cooled. The reaction is shown to have completed within 0.4 s.

3.4.2. $3Hf + B_4C \rightarrow 2HfB_2 + HfC$ combustion. This reaction has a combustion front velocity of 5 mm s^{-1}. From Table 1, T_{ad} of this combustion also falls between those of the individual HfC and HfB_2 from the respective elements shown in §3.2.3 and §3.3.3. Because Hf has a higher Z (thus higher scattering power) than Zr, each frame was adequately recorded with an integration time of 100 ms. The TRXRD patterns are shown in Fig. 13. At t = 0.0 s, the reaction was triggered and the reactant Hf(100), Hf(002), Hf(101) and Hf(102) peaks were recorded at 373 K. At t = 1.1 s, the Hf metal peaks broadened, indicating the arrival of the combustion front in the probed area. The HfB_2(101) peak appeared first at t = 1.2 s, followed by the HfC peaks at t = 1.3 s, co-existent with the diminishing reactant Hf metal. At t = 1.4 s onwards, only the products HfC and HfB_2 persisted with a slight shift to high 2θ values. The combustion was completed within 0.2 s.

3.4.3. $3Ta + B_4C \rightarrow 2TaB_2 + TaC$ combustion. From Table 1, it is shown that this reaction has a lower combustion front velocity of 2 mm s^{-1}, and an adiabatic temperature of 2476 K, which is well below the melting points of all the reactants and products: Ta (3290 K), B_4C (2623 K), TaB_2 (3270 K) and TaC (4150 K) (Weast & Astle, 1982). Hence, the reaction is truly a solid combustion involving no liquid phase. Fig. 14 shows the TRXRD patterns. At t = 4.3 s, the TaB_2(101) appeared, co-existing with Ta(110). At t = 4.4 s, both TaB_2(100) and Ta(101) are evident. At t = 4.6 s, a third TaB_2(001) peak appeared as well as the TaC(200) peak. The product–reactant co-existed until t = 4.8 s. From t = 4.9 s onwards, only the product peaks remained and moved to high 2θ values due to lattice contraction as the sample cooled. The combustion completed in 0.6 s.

4. Concluding remarks

By using a 2-inch photodiode array and an increase in the solid angle of acceptance to the detector coupled with a more precise diffraction geometry, we have expanded a former 6° 2θ

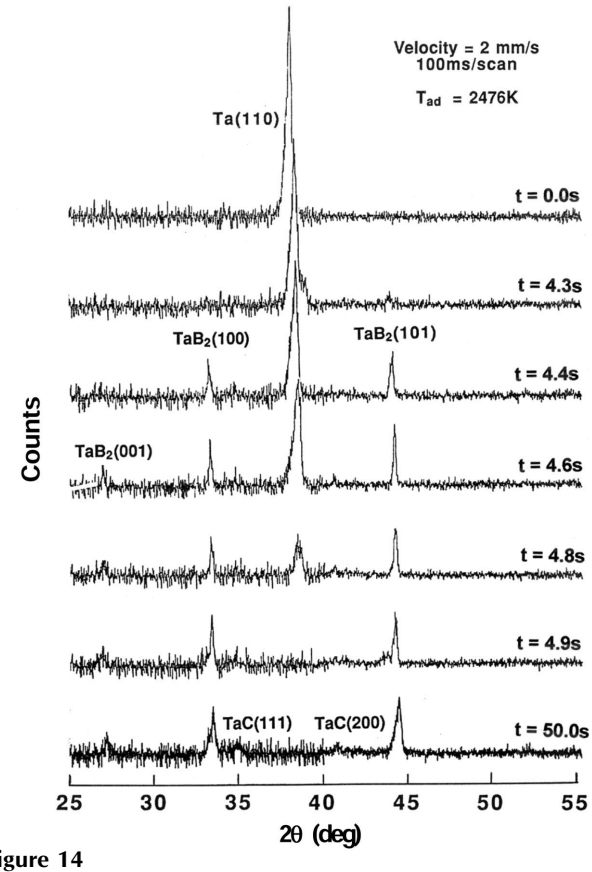

Figure 14
TRXRD patterns for the $3Ta + B_4C \rightarrow 2TaB_2 + TaC$ reaction, showing the sequence of critical events during the combustion. The combustion was completed within 0.6 s, with also a low combustion front velocity of 2 mm s^{-1}.

window space (Wong *et al.*, 1990; Larson *et al.*, 1993) to 30°. This increase greatly facilitates identification of the reaction product and any intermediates in the combustion fronts of a selected series of refractory metal carbides and di-borides from the corresponding elemental constituents as well as the binary products from the metals and B_4C. Experimental time resolution down to 100 ms has been found adequate to furnish diffraction signals with good signal-to-noise ratio for phase identification. Our findings are summarized in the following.

Within a time resolution of 100 ms, no intermediate was detected in any of the combustion systems denoted by (i) $M + C \rightarrow MC$; (ii) $M + 2B \rightarrow MB_2$; and (iii) $3M + B_4C \rightarrow 2MB_2 + MC$, where M = Ti, Zr, Nb, Hf or Ta. This is contrasted with the $Ta + C \rightarrow TaC$ combustion system studied earlier (Larson *et al.*, 1993) in which a discernable intermediate sub-carbide, Ta_2C phase, formed first, reacted further and disappeared to yield the final TaC product.

The combustions involving Ti, Zr and Hf have estimated high adiabatic temperatures T_{ad} and are expected to exhibit a liquid phase of the metal at the combustion front as are evident from (i) the known melting points of the metal, metal carbides and metal diborides (Weast & Astle, 1982), (ii) the absence of any Bragg peaks in the Zi + 2B system at t = 3.2 s shown in Fig. 9, and (iii) the normalized intensity profile for the $Ti + C \rightarrow TiC$ combustion shown in Fig. 5.

The Nb and Ta systems, however, have lower T_{ad} that are well below the respective melting points of the metal reactants or products. These two combustions are truly solid combustions involving no liquid phase. Accordingly, the combustion front velocity was also lower (Table 1) compared with those of the Ti, Zr and Hf systems. The combustion front velocity is a direct measure of the reaction rate which is enhanced by the presence of a liquid phase due to diffusion enhancement in the liquid phase.

These results clearly demonstrate the usefulness of the TRXRD technique using intense synchrotron radiation to monitor phase transformation and high-temperature solid-state processes down to the 100 ms time regime not readily possible with conventional means. Improved experimentation methods such as a smaller beam spot emitted from third-generation synchrotron sources, better mechanical stability (tighter scattering geometry) and use of an area detector would enable more quantitative structural information for future materials dynamic studies exemplified by this work.

This work was performed under the auspices of the US Department of Energy (DOE), Lawrence Livermore National Laboratory, under contract W-7405-ENG-48. We would like to thank J. B. Holt for introducing the authors to the field combustion synthesis; and G. Lamble, J. Scrofani and L. Fareria for technical assistance on beamline X11-A at Brookhaven NSLS, operated by the US Department of Energy, Division of Chemical Sciences.

References

Aleksandrov, V. V. & Korchagin, M. A. (1987). *Fiz. Goreniya Vzryva*, **23**, 55–63. [English translation in *Combust. Explos. Shocks Waves USSR* (1987). **23**, 557–564.]
Barin, I. & Knacke, O. (1973). *Thermochemical Properties of Inorganic Substances.* Berlin: Springer-Verlag.
Barin, I., Knacke, O. & Kubaschewski, O. (1977). *Thermochemical Properties of Inorganic Substances (Suppl.).* Berlin: Springer-Verlag.
Boldyrev, V. V. & Aleksandrov, V. (1981). *Dok. Akad. Nauk. SSSR*, **259**, 1127–1232.
Feng, A. & Munir, Z. A. (1995). *Metall. Mater. Trans.* **26**B, 581–593.
Frahm, R., Wong, J., Holt, J. B., Larson, E. M., Rupp, B. & Waide, P. (1992). *Phys. Rev. B*, **46**, 9205–9207.
Gedevanishvili, S. & Munir, Z. A. (1995). *J. Mater. Res.* **10**, 2642–2647.
Heald, S. M., Pick, M., Tranquada, J. M., Sayers, D. E.. Budnick, J. I., Stern, E. A., Wong, J., Stuckey, G., Chester, A., Woolery, G. & Morrison, T. (1986). *Nucl. Instrum. Methods*, A**246**, 120–124.
Hirao, K., Miyamoto, Y. & Koizumi, M. (1987). *J. Ceram. Soc. Jpn Int. Ed.* **95**, 905–910.
Larson, E. M., Waide, P. A. & Wong, J. (1991). *Rev. Sci. Instrum.* **62**, 53–57.
Larson, E. M., Wong, J., Holt, J. B., Waide, P. A., Nutt, G. & Rupp, B. (1993). *J. Mater. Res.* **8**, 1533–1541.
Lebrat, L.-P. & Varma, A. (1991). *Physica C*, **184**, 220–228.
Merzhanov, A. G. (1974). *Arch. Procesow Spalania*, **5**, 17–39. [English translation (*Theory of Gasless Combustion*) available as LLL reference 03008 from LLNL Library, PO Box 808, Livermore, CA 94550, USA.]

Merzhanov, A. G. (1990*a*). *Ceram. Trans.* **13**, 519.
Merzhanov, A. G. (1990*b*). *Combustion and Plasma Synthesis of High-Temperature Materials*, edited by Z. A. Munir & J. B. Holt, pp. 1–53. New York: VCH.
Merzhanov, A. G. & Borovinskaya, I. P. (1972). *Dokl. Akad. Nauk SSSR*, **204**, 366–374.
Munir, Z. A. (1988). *Ceram. Bull.* **67**, 342–354.
Munir, Z. A. & Anselmi-Tamburini, U. (1989). *Mater. Sci. Rep.* **3**, 277–284.
Munir, Z. A. & Holt, J. B. (1990). *Combustion and Plasma Synthesis of High-Temperature Materials.* New York: VCH.
Naiborodenko, Yu. S. & Itin, V. I. (1975). *Fiz. Goreniya Vzryva*, **11**, 343–353; ibid, **11**, 734–738.
Novikov, N. P., Borovinskaya, I. & Merzhanov, A. G. (1975). *Protesessy Goreniya v Khimicheskoyoi Tekhnologii I Metallurgii (Combustion Processes in Chemical Engineering and Metallurgy)*, edited by A. G. Merzhanov, Chernogolovka, USSR, pp. 174–188. [English translation (*Thermodynamic analysis of Self-Propagating High-Temperature Synthesis Reactions*) available as LLL reference 03007 from LLNL Library, PO Box 808, Livermore, CA 94550, USA.]
Rupp, B., Holt, J. B. & Wong, J. (1992). *CALPHAD*, **16**, 377–386.
Rupp, B., Wong, J., Holt, J. B. & Waide, P. (1994). *J. Alloys Compds*, **209**, 25–33.
Shon, I. J., Munir, Z. A., Yamazaki, I. & Shoda, K. (1996). *J. Am. Ceram. Soc.* **79**, 1875–1880.
Villars, P. & Calvert, L. D. (1985). *Pearson's Handbook of Crystallographic Data for Intermediate Phases*, Vols. 1–3. Metals Park, OH: ASM.
Weast, R. C. & Astle, M. J. (1982). Editors. *Handbook of Chemistry and Physics*, 62nd ed., pp. B73–B166. Boca Raton, FL: CRC Press.
Wong, J., Larson E. M., Holt, J. B., Waide, P., Rupp, B. & Frahm, R. (1990). *Science*, **249**, 1406–1409.
Wyckoff, R. W. G. (1963). *Crystal Structure*, Vol. 1. New York: Interscience.
Xue, H. & Munir, Z. A. (1996). *Metall. Mater. Trans.* **27**B, 475–480.
Yamada, O., Miyamoto, Y. & Moizumi, M. (1987). *J. Am. Ceram. Soc.* **70**, C206–C208.